Nature of the octahedral tilting phase transitions in perovskites: A case study of $CaMnO_3$

Johan Klarbring* and Sergei I. Simak
Department of Physics, Chemistry and Biology (IFM), Linköping University, SE-581 83 Linköping, Sweden

(Received 13 October 2017; published 17 January 2018)

The temperature-induced antiferrodistortive (AFD) structural phase transitions in $CaMnO_3$, a typical perovskite oxide, are studied using first-principles density functional theory calculations. These transitions are caused by tilting of the MnO_6 octahedra that are related to unstable phonon modes in the high-symmetry cubic perovskite phase. Transitions due to octahedral tilting in perovskites normally are believed to fit into the standard soft-mode picture of displacive phase transitions. We calculate phonon-dispersion relations and potential-energy landscapes as functions of the unstable phonon modes and argue based on the results that the phase transitions are better described as being of order-disorder type. This means that the cubic phase emerges as a dynamical average when the system hops between local minima on the potential-energy surface. We then perform *ab initio* molecular dynamics simulations and find explicit evidence of the order-disorder dynamics in the system. Our conclusions are expected to be valid for other perovskite oxides, and we finally suggest how to predict the nature (displacive or order-disorder) of the AFD phase transitions in any perovskite system.

DOI: 10.1103/PhysRevB.97.024108

I. INTRODUCTION

Materials with crystal structures related to the aristotype cubic perovskite are one of the most intensively studied class of materials. Common subclasses include the oxide ABO_3 and halide ABX_3 ($X = \mathrm{F,Cl,Br,I}$) pervoskites. Varying the occupying ion (or molecule) on the A and B sites within these subclasses produces inorganic (or inorganic-organic hybrid) perovskite materials with a wide range of attractive properties. As a result, they have found use in diverse applications ranging from fuel cells and catalysis to thermoelectrics and solar cells [1–5].

Many perovskites undergo one or several phase transitions upon heating where the low-symmetry phases at low temperatures are related to the high-temperature cubic perovskite by simple phonon instabilities. One common type is ferroelectric (FE) transitions, which, in the case of ABO_3 oxides, involves off centering of the B-site cation inside the BO_6 octahedra, typically related to an imaginary phonon mode at the Γ point of the first Brillouin zone (BZ) of the cubic perovskite structure. A second class of phase transitions, known as antiferrodistortive (AFD) transitions, involve rotations, or tilts, of the BO_6 octahedra around one or several of the [100] axes of the cubic structure. These transitions are a result of unstable phonon modes at the M and R points of the BZ, corresponding to in-phase (ip) and out-of-phase (oop) rotations of successive BO_6 octahedra, respectively (see Fig. 1).

These phase transitions are often detrimental to the operation in the prospective applications. An example is the perovskite oxide $CaMnO_3$ (CMO), which is a promising material, e.g., for high-temperature thermoelectric applications. There the thermoelectric figure of merit ($ZT = \frac{\sigma S^2 T}{\kappa}$, where σ is the electrical conductivity, S is the Seebeck coefficient, T is the temperature, and κ is the thermal conductivity) drops sharply across the AFD phase transitions [6]. The ability to predict the occurrence and describe the nature of these transitions thus becomes of considerable importance.

The mechanism by which these phase transitions occur can be classified broadly as being of displacive or order-disorder type [8]. In the former case the low-temperature phases are obtained simply by "freezing in" one or several unstable phonon modes into the high-symmetry structure. In the latter case, the system stays in the low-symmetry phase on the time scale of the thermal vibrations even above the transition temperature, and the high-temperature high-symmetry phase emerges as a dynamical average when anharmonic thermal excitations cause the system to sample many different local minima on the potential-energy surface (PES). In the case of AFD transitions these local minima correspond to different tilt configurations of the BO_6 octahedra. In many cases transitions may show characteristics of both order-disorder and displacive types.

FE transitions often have both order-disorder and displacive characteristics [9,10], whereas the octahedral tilting (AFD) transitions have mostly been considered to be of pure displacive character [11], although order-disorder dynamics have also sometimes been suggested [12–15]. A notable recent example is the hybrid perovskite methylammonium lead iodide ($CH_3NH_3PbI_3$) where an order-disorder mechanism was attributed to its tetragonal-to-cubic phase transition [16].

Here it should be noted that it is notoriously difficult to experimentally distinguish between displacive and order-disorder transitions in perovskites. Mainly because many of the common experimental techniques have a time resolution much longer than the average time the system stays in any one local minimum on the PES and hence will only reveal the average structure. This is therefore a situation where theoretical simulations can provide detailed insights not easily accessible to experiment.

*johan.klarbring@liu.se

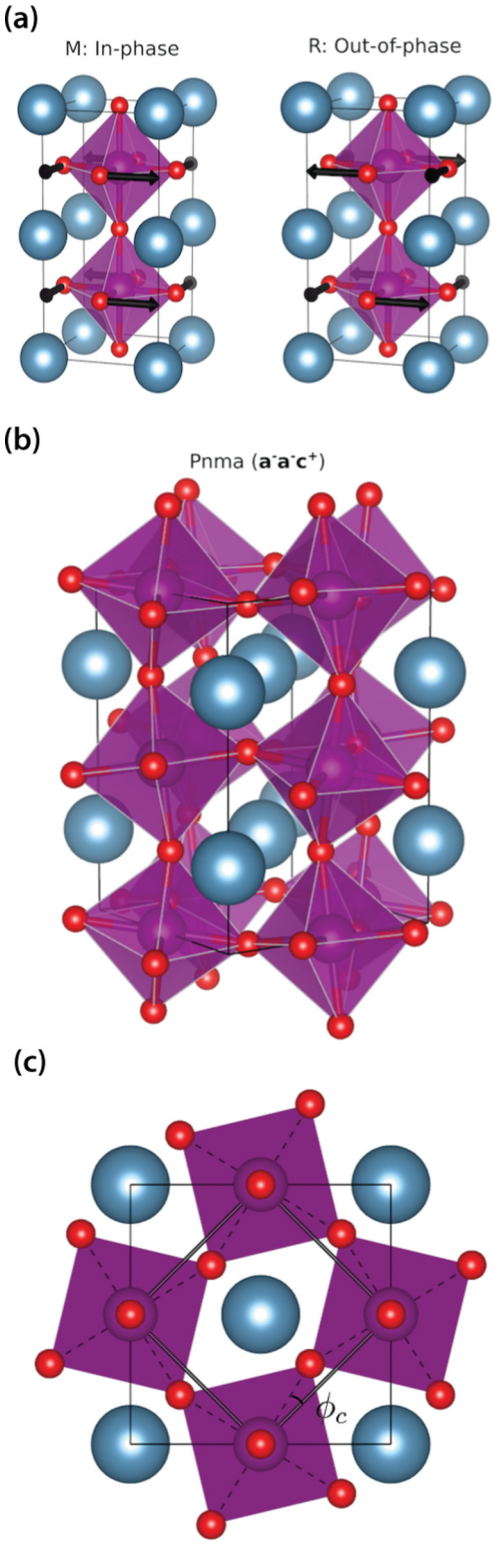

FIG. 1. (a) The two unstable octahedral tilting modes in the cubic perovskite structure. (b) The orthorhombic ground-state structure of $CaMnO_3$ (CMO) (space-group $Pnma$) where the octahedra are tilted oop around the pseudocubic a and b axes and ip around the c axis. This corresponds to the tilt configuration $a^-a^-c^+$ in Glazer notation [7]. (c) The view along the c axis, showing the definition of the tilt angle around this axis ϕ_c. Ca and O ions are represented by light blue and red spheres, respectively, whereas the Mn ions are in the center of the pink MnO_6 octahedra.

In this paper, we study CMO as an example system and investigate in detail the nature of its AFD phase transitions. The ground state is orthorhombic with space-group $Pnma$. This structure is related to the cubic perovskite by an oop tilt of the BO_6 octahedra around two of the cubic coordinate axes and an ip tilt around the third axis. This is conveniently expressed as $a^-a^-c^+$ in Glazer notation [7], which is described in detail in Sec. II. When heated in air $CaMnO_3$ undergoes two temperature-induced AFD structural phase transitions [17], first to a tetragonal structure, presumably space-group $I4/mcm$ and tilt configuration $a^0a^0c^-$ at $T_c \approx 1170$ K and finally to the ideal cubic structure $a^0a^0a^0$ at $T_c \approx 1190$ K.

We use static density functional theory (DFT) to calculate harmonic phonons and potential-energy landscapes of combinations of the unstable octahedral tilting modes. We show, based on these results and experimental transition temperatures, how it is possible to predict the nature (displacive or order-disorder) of AFD phase transitions in pervoskite systems. In CMO our results clearly indicate an order-disorder transition mechanism. We finally perform *ab initio* molecular dynamics (AIMD) simulations where the order-disorder mechanism is seen clearly in the form of fluctuations between different tilt configurations in the system.

II. METHODOLOGY

Throughout this paper we will use Glazer's notation [7] to describe the tilt configurations of the MnO_6 octahedra around the pseudocubic axes. In this notation a tilt pattern is specified with three letters with associated superscripts. The letters, a, b, or c denote tilts around the three pseudocubic lattice vectors. If two letters are the same, the tilt angles around those axes are of equal magnitude. The superscripts $+$ and $-$ signify that rotations of sequential octahedra along the corresponding axis is taken in phase and out of phase, respectively, whereas the superscript 0 signifies the absence of a tilt around the corresponding axis. For example, the $Pnma$ structure has the Glazer tilt configuration $a^-a^-c^+$ signifying oop tilts of equal magnitude around the a and b axes and an ip tilt around the c axis. We note that the structures are not completely determined by the tilts and we will take a certain Glazer tilt pattern, when appropriate, to also include any further relaxations of both ions and lattice vectors consistent with the space-group symmetry of the structure in question.

The $Pnma$ and $I4/mcm$ structures have lattice vectors $\mathbf{a}_t$, $\mathbf{b}_t$, and $\mathbf{c}_t$ related to the pseudocubic lattice vectors $\mathbf{a}_c$, $\mathbf{b}_c$, and $\mathbf{c}_c$ as

$$\begin{pmatrix} \mathbf{a}_t \\ \mathbf{b}_t \\ \mathbf{c}_t \end{pmatrix} = \begin{pmatrix} -1 & 1 & 0 \\ 1 & 1 & 0 \\ 0 & 0 & 2 \end{pmatrix} \begin{pmatrix} \mathbf{a}_c \\ \mathbf{b}_c \\ \mathbf{c}_c \end{pmatrix} \tag{1}$$

[see Fig. 1(b)]. We will refer to this unit cell as the tetragonal unit cell.

In the AIMD simulations the tilt angle ϕ_i of an Mn-O bond, represented by the vector $\mathbf{r}^{\mathrm{MnO}}(t)$, around a pseudocubic axis i ($i = a,b,c$) at time t was calculated as the angle between the projection of $\mathbf{r}^{\mathrm{MnO}}(t)$ onto the plane orthogonal to i and the ideal Mn-O bond vector [see Fig. 1(c)]. The tilt angle of an

octahedron is then obtained by averaging over the four relevant Mn-O tilt angles corresponding to that octahedron and axis.

The DFT calculations were performed in the Vienna *ab initio* simulation package (VASP) [18–20] using the projector augmented-wave (PAW) [21] method. Following Ref. [22], we treat exchange and correlation effects using the PBEsol [23] form of the generalized gradient approximation and apply a $U = 3$ eV effective Hubbard correction to the Mn $3d$ states [24]. We used PAW potentials that treat the Ca $3p4s$, Mn $3d4s$, and O $2s2p$ states as valence.

Born-Oppenheimer MD simulations were performed in the canonical (NVT) ensemble with the temperature controlled by a Nosé-Hoover thermostat with the default Nosé mass parameter as set by VASP and a 2-fs time step. We use a $2 \times 2 \times 2$ repetition of the 20-atom tetragonal unit cell, 160 atoms in total. The three cell vectors are fixed at the ratio $\sqrt{2} \times \sqrt{2} \times 2$, making it essentially equivalent to a cubic supercell. The deviations of the stress tensor from a hydrostatic form in this supercell are small (< 0.5 GPa) when the volume is adjusted to keep the average of all components of the stress tensor < 0.5 GPa.

The Kohn-Sham orbitals were expanded in plane waves up to a kinetic-energy cutoff of 800 and 600 eV for the static and MD simulations, respectively. In all static calculations the first Brillouin zone was sampled on a $8 \times 8 \times 6$ Monkhorst-Pack grid of k points for the primitive tetragonal cell. The grid was reduced appropriately when the supercell was enlarged. A $2 \times 2 \times 1$ grid was used for the MD simulations of the 160-atom supercell. Relaxations were performed until all ionic forces in the system were smaller than 0.0001 eV/Å for the three considered phases.

The phonon calculations were performed using the small displacement method as implemented in the PHONOPY [25] software package using the default displacement distance 0.01 Å. These calculations were performed in $2 \times 2 \times 2$ expansions of the tetragonal unit cell for the $Pnma$ and $I4/mcm$ structures and a $2 \times 2 \times 2$ (40-atom) cubic supercell for the cubic $Pm\bar{3}m$ structure.

PESs as functions of various unstable octahedral tilting modes were calculated in a 40-atom unit cell constructed as a $2 \times 2 \times 2$ expansion of the cubic unit cell. Energies were calculated on a 14×14 grid with varying (positive) amplitudes of the octahedral tilts. The energies on this grid were then interpolated and finally mirrored in the tilt-coordinate axes to produce the final energy landscapes (Fig. 4).

Minimum energy paths between equilibrium tilt configurations were calculated using the generalized solid-state nudged elastic band (GSSNEB) method [26], which takes into account both atomic and unit-cell degrees of freedom.

For all static calculations we imposed the known low-temperature G-type antiferromagnetic (AFM) ordering of the Mn magnetic moments, i.e., both intraplane and interplane couplings are AFM and accordingly all neighboring Mn moments are oppositely aligned. We simulate the high-temperature paramagnetic (PM) phase of CMO using the disordered local moments [27–36] approach where the magnetic disorder is modeled by randomly distributed collinear magnetic moments. In our case this entails initiating the simulations with Mn magnetic moments distributed in a special quasirandom (SQS) sense [37] where an equal number of atoms is given up and down spins. According to Ref. [38] this is a valid approximation of the PM phase as long as the relaxation energy when switching from the AFM to the SQS distribution of the magnetic moments is

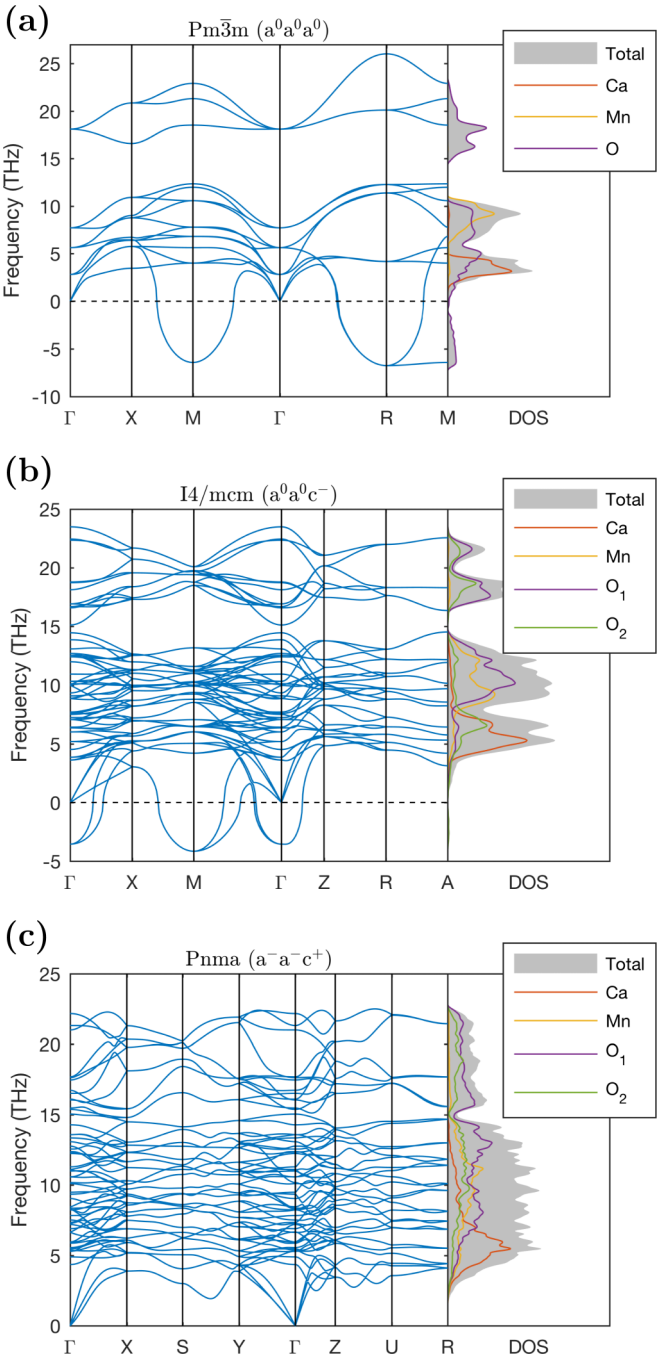

FIG. 2. Total and site-projected phonon density of states and dispersion relations along selected paths in the first BZ for the (a) cubic $Pm\bar{3}m$, (b) tetragonal $I4/mcm$, and (c) orthorhombic $Pnma$ phases of CMO.

small. This criterion is fulfilled in the present case where this relaxation energy is calculated to be ∼2 meV/Mn atom. In any case, since the structural phase transitions in CMO occur at temperatures ∼1000 K above the Néel temperature $T_N = 124$ K [39], it is highly unlikely that the magnetic order-disorder has any explicit influence. We checked this by redoing selected simulations with G-type AFM and ferromagnetic ordering. In all the tests the results were qualitatively unaffected.

III. RESULTS AND DISCUSSION

A. Ground-state structures and harmonic phonons

We start by investigating the ground-state (0 K) structural and vibrational properties of the orthorhombic $Pnma$, tetragonal $I4/mcm$, and cubic $Pm\bar{3}m$ structures with G-type AFM ordering. The relaxed lattice parameters and relative energies are given in Table I. The $Pnma$ and $I4/mcm$ structures are 66 and 46 meV/atom more stable than the cubic $Pm\bar{3}m$ structure, respectively. As expected $Pnma$ is the lowest in energy by a significant amount, in agreement with it being the stable phase at low temperatures.

Next, we investigate the dynamical stability of the three structures in the harmonic approximation at 0 K. Figure 2(a) shows the phonon-dispersion relation of the cubic structure. As is typical of many perovskite structures with a $Pnma$ ground state the structure exhibits large unstable phonon modes at the M and R points of the first BZ. As mentioned above, these modes correspond to ip and oop tilts of successive MnO_6 octahedra, respectively, and the $Pnma$ structure can be thought of as resulting from freezing in a suitable combination of these two modes into the cubic structure.

We note that there is some discrepancy in the literature regarding a soft FE mode at the Γ point in the cubic phase of CMO. Although Refs. [41,42] report this mode to be imaginary at the equilibrium volume, Refs. [22,43] report no such instability at equilibrium volume and with the G-type AFM ordering. The presence of a weak FE instability in the cubic phase of perovskite oxides with AFD instabilities is quite common, and in many cases, such as the present one, the AFD instability is much stronger and completely dominates over the FE instability.

Figures 2(b) and 2(c) show the phonon-dispersion relation and DOS of the $I4/mcm$ and $Pnma$ structures, respectively. The $I4/mcm$ phase has imaginary modes at the M and Γ points. These two modes mainly consist of ip and oop rotations, respectively, of MnO_6 octahedra, and the structure is thus, like the cubic structure, unstable to both types of octahedral tilts. This is an intuitive result considering that the cubic structure is unstable to both tilt types and that the $I4/mcm$ is related to the cubic phase by oop tilt around a single pseudocubic axis.

The $Pnma$ structure, on the other hand, shows no imaginary frequencies throughout the BZ and thus is dynamically stable at 0 K, again consistent with it being the ground-state structure of CMO.

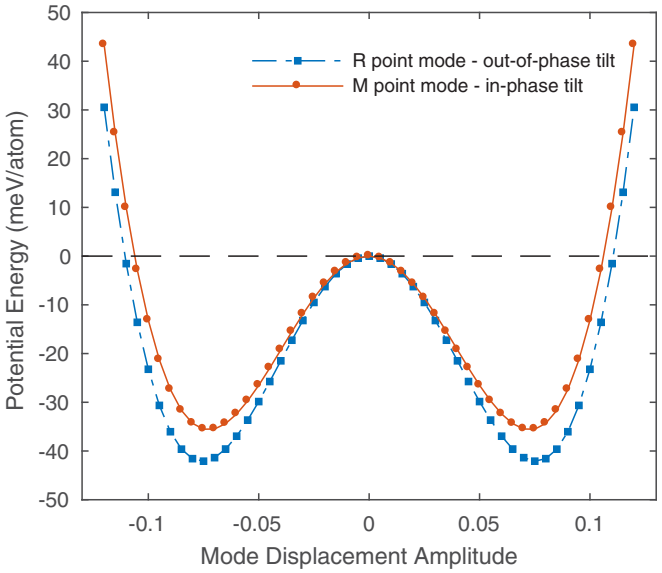

FIG. 3. Potential energy as a function of the amplitude of the unstable M-point ip (the red circles) and R-point oop (the blue squares) tilting modes in the cubic perovskite structure. The mode amplitude (tilts) are given as the offset distance of a single O ion in units of the lattice constant of the cubic perovskite. The lines are guides for the eye.

B. Potential-energy landscapes

To move beyond the harmonic approximation we separately freeze in the two soft tilt modes into the ideal cubic structure and calculate the potential energies as functions of their amplitude. The results are presented in Fig. 3 where we see that the energy curves are typical double-well potentials. This is to be expected from the harmonic phonon-dispersion relations

TABLE I. Lattice parameters and relative energies (with respect to the cubic structure) of the orthorhombic $Pnma$, tetragonal $I4/mcm$, and cubic $Pm\bar{3}m$ structures. G-type AFM ordering was considered for all three structures. For the $Pnma$ and $I4/mcm$ structures the pseudocubic lattice vectors are related to their respective unit-cell vectors by Eq. (1). Experimental values at room temperature for the orthorhombic phase [40] are provided for comparison.

		Pseudocubic cell parameters			
Structure (space group)	Tilt configuration	a (Å)	b (Å)	c (Å)	ΔE (meV/atom)
Cubic ($Pm\bar{3}m$)	$a^0a^0a^0$	3.727			0
Tetragonal ($I4/mcm$)	$a^0a^0c^-$	3.678		3.792	−47
Orthorhombic ($Pnma$)	$a^-a^-c^+$	3.702	3.737	3.711	−66
Experiment ($Pnma$)		3.725	3.736	3.729	

(Fig. 2). The depths of these potentials are 36 and 42 meV/atom for the *ip* and *oop* tilts, respectively. Allowing for relaxation of the lattice vectors and Ca ions deepens the potential wells by ∼5 meV/atom in both cases and shifts the minima to slightly larger amplitudes.

These types of one-dimensional (1D) double-well potentials are often used to analyze octahedral tilting transitions in perovskites [44,45]. The depth of the potential well has, for instance, been used as an indicator of the nature of the phase transitions, i.e., deep and shallow wells should correspond to order-disorder and displacive transitions, respectively.

One of the most common perovskite variant is the *Pnma*, $a^-a^-c^+$ structure. Materials with this structure normally sequentially lose their tilts via a series of temperature-induced phase transitions, finally ending up in the ideal cubic structure at high temperatures.

Care should be taken when analyzing this type of transition in terms of 1D double-well potentials since, if there are tilts around several axes present in the system, treating the different tilts using separate double-well potentials is only physically reasonable if the different tilting modes are effectively independent of each other. This would mean, for instance, that the double well corresponding to the *ip* tilt in Fig. 3 should essentially be unchanged if the tilt is performed not in the cubic structure but in a system with other tilts present.

To investigate this point, we next calculated PESs as functions of several different tilts in the system, i.e., essentially freezing in combinations of the *M*- and *R*-point soft phonon modes with varying amplitudes into the structure. We allow for full relaxation of both the cell parameters and the Ca ions. We note that the Mn ions are fixed in the center of the MnO_6 octahedra by symmetry.

Figure 4(a) shows the PES in the $a^-a^-c^+$ tilt system. Note that in this tilt system there are two degrees of freedom since the two *oop* tilts (a^-) are of equal amplitude. The four local minima correspond to symmetry equivalent equilibrium tilt amplitudes of the *Pnma* structure, and the origin is the cubic tiltless structure. The depth of these minima is 64 meV/atom, which corresponds to the difference in energy between the cubic and the *Pnma* structures. Note that the small ∼2 meV/atom discrepancy between this energy difference and the one given in Table I comes from the relaxations of oxygen ions that are not rigid tilts of the octahedra but still allowed by the *Pnma* symmetry.

Performing an *ip* tilt in the presence of the two a^- *oop* tilts, denoted $a^-a^-c^+ \rightarrow a^-a^-(-c)^+$, gives the double-well potential traced out when going horizontally between two minima in Fig. 4(a). The depth of this double well is ∼11 meV/atom, this is ∼3 times smaller than the depth of the corresponding well when performing the *ip* tilt switch directly in the cubic structure.

In Fig. 4(b) we have fixed one of the *oop* tilts to its value at the minimum, taken from Fig. 4(a) and then calculated the PES as a function of the remaining two tilts. Note that the origin corresponds to the $a^-b^0b^0$ (equivalent to $a^0a^0c^-$) structure in this case and not to the cubic $a^0a^0a^0$ structure. The four minima again correspond to the equilibrium tilt amplitudes in the *Pnma* structure. Going vertically between two minima in Fig. 4(b) corresponds to performing an *oop* tilt in the presence of one *ip* and one *oop* tilt, i.e., a path $a^-a^-a^+ \rightarrow a^-(-a)^-c^+$, the depth of the double well thus traced out is also ∼11 meV/atom. This is again remarkably different from the result obtained by performing the *oop* tilt switch directly in the cubic structure.

It is clear then that the energy cost for a tilt switch is drastically reduced when other tilts are present in the system since the paths do not go over the high-energy cubic structure. This conclusion is unlikely a feature of just CMO but should

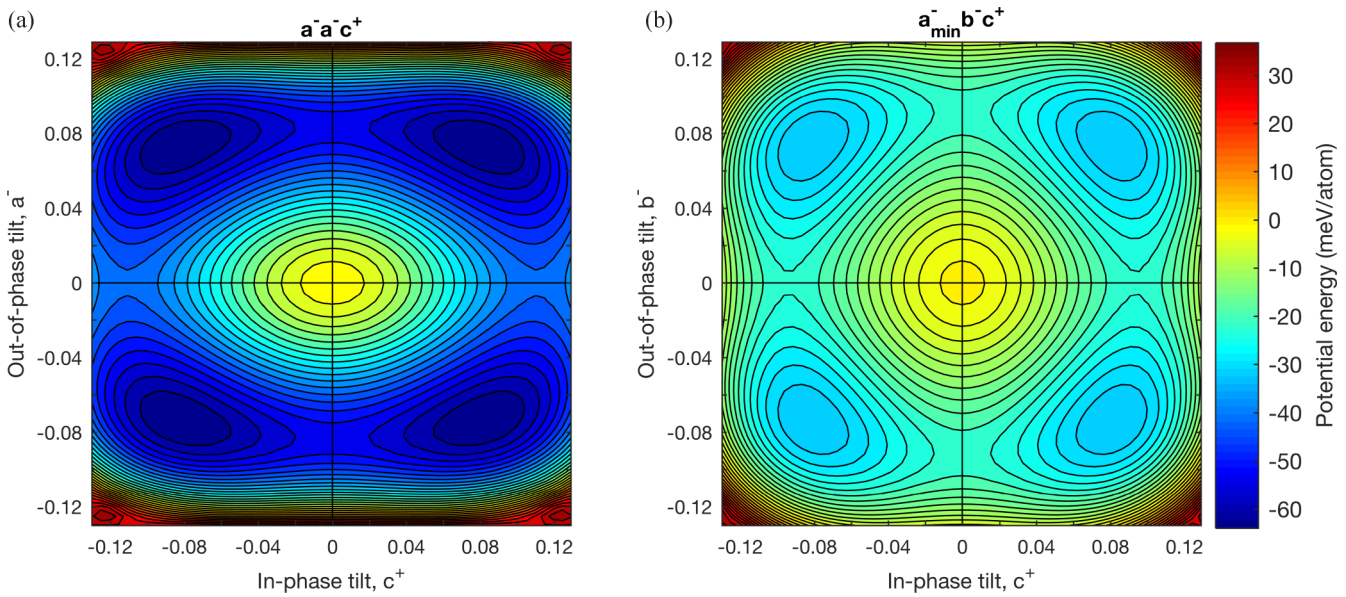

FIG. 4. Potential-energy landscapes as functions of the amplitude of octahedral tilts in the cubic perovskite structure. The tilts are given as the offset distance of a single O ion in units of the lattice constant of the cubic perovskite. In (a) the *oop* tilts around the pseudocubic *a* and *b* axes are fixed to be of the same magnitude, whereas in (b) the *oop* tilt around the pseudocubic *a* axis is fixed at its minimum values from (a) and the remaining *oop* and *ip* tilts are varied. Relaxations of both the cell vectors and the Ca ions are included.

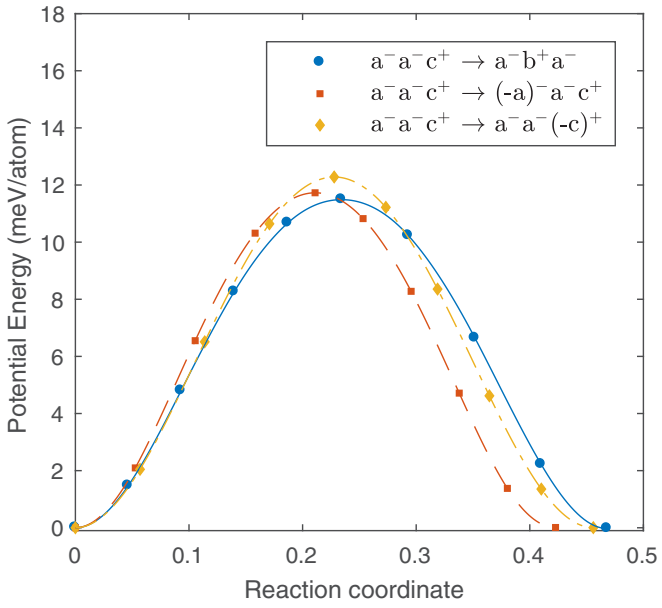

FIG. 5. GSSNEB minimum energy path between equivalent $(a^-a^-c^+)$-type tilt configurations. The reaction coordinate is the cumulative distance along the path divided by $\sqrt{N}$ where N is the number of atoms.

be expected to hold for other perovskites with a ground state containing tilts around several axes. We thus advise caution in using 1D double-well potentials to analyze the AFD transitions in such perovskites.

We have also calculated the minimum energy barriers for the two tilt switches described above in the fully relaxed $Pnma$ structures using the GSSNEB method [26]. The resulting energy curves are shown in Fig. 5. The barriers and the paths correspond closely to the ones from Fig. 4. We note again that the minima in Fig. 4 are $\sim$2 meV/atom too shallow due to the absence of relaxations of the oxygen ions beyond the rigid octahedral tilts. This makes the minimum energy paths in Fig. 5 slightly higher than the ones obtained directly from Fig. 4.

We briefly comment on the symmetry of the $a^-a^-c^+ \rightarrow a^-a^-(-c)^+$, $a^-a^-c^+ \rightarrow a^-(-a)^-c^+$ transition paths. The paths obtained from Fig. 4 naturally stay in the $a^-a^-c^+$ ($Pnma$) symmetry during most of the paths, but the maximum is the higher-symmetry $a^-a^-c^0$ ($Imma$) and $a^-b^0c^+$ ($Cmcm$) structures, respectively, for the two cases. In the GSSNEB calculations the symmetry is turned off, but we note that the maxima on the two corresponding paths still pass very close to the same higher-symmetry structures, indicating that the minimum energy paths are essentially those obtained from Fig. 4.

Another path between two equivalent $a^-a^-c^+$ tilt configurations is for the tilt sequence around one of the oop tilt axes to change to ip and the ip sequence to oop, corresponding to a transition of the type $a^-a^-c^+ \rightarrow a^-b^+a^-$. The corresponding GSSNEB minimum energy path is shown in Fig. 5.

We thus see that there exist many paths of three distinct types: $a^-a^-c^+ \rightarrow a^-a^-(-c)^+$, $a^-a^-c^+ \rightarrow a^-(-a)^-c^+$, and $a^-a^-c^+ \rightarrow a^-b^+a^-$ with very similar energy barriers between symmetry equivalent $Pnma$ structures.

C. Discussion: Displacive vs order-disorder phase transitions and comparison to experiments

We now investigate to what degree the calculated potential energies in the previous section are commensurate with a displacive or order-disorder description of the phase transitions and with the experimentally observed transition temperatures.

The experimentally proposed phase-transition sequence in CMO is [17] as follows:

$$\underset{(a^-a^-c^+)}{Pnma} \xrightarrow{\sim 1170\,\mathrm{K}} \underset{(a^0a^0c^-)}{I4/mcm} \xrightarrow{\sim 1190\,\mathrm{K}} \underset{(a^0a^0a^0)}{Pm\bar{3}m},$$

where it should be noted that the transition temperatures vary with, among other things, oxygen deficiency. A few other things should be noted here: (1) Several experimental works have confirmed the presence of two structural phase transitions [46,47], whereas some other studies [48,49] find only a single orthorhombic-to-cubic phase transition without an intermediate tetragonal phase. The existence of the intermediate phase is likely related to oxygen deficiency [47]. In fact straightforward extrapolation of Fig. 3 in Ref. [47] indicates that the intermediate tetragonal phase should be absent at perfect oxygen stoichiometry, which is the case treated in this paper. We may thus expect our results to be consistent with a single $a^-a^-c^+ \rightarrow a^0a^0a^0$ transition. (2) Reference [17] is, to our knowledge, the only work which performed structural characterizations for all three phases. In this context we point out that the determination of the phase-transition sequence in several other perovskite oxides, e.g., $SrZrO_3$ [50], have been revised several times, indicating the difficulty of the experimental task.

We first consider the direct orthorhombic-to-cubic transition in the case of a pure displacive phase-transition mechanism. Displacive transitions occur once the thermal energy of the system becomes hight enough so that the relevant energy wells become effectively negligible. In this case one would expect an intermediate $a^-a^-c^+ \rightarrow a^-a^-c^0$ or $a^-a^-c^+ \rightarrow a^-b^+c^0$ displacive transition since the corresponding energy wells are significantly smaller compared to going directly to the $a^0a^0a^0$ structure.

In the case where an intermediate tetragonal phase exists, a displacive $a^-a^-c^+ \rightarrow a^-b^0b^0$ transition can be seen as the movement from one of the minima to the origin in Fig. 4. In the same way as above, there should exist an intermediate $a^-b^+c^0$ or $a^-a^-c^0$ phase. Moving on to the second ($a^-b^0b^0 \rightarrow a^0a^0a^0$) transition we note that this transition is observed to happen just $\sim$20 K above the first one whereas the remaining energy well that needs to be overcome for the displacive transition to occur has a significant depth of 47 meV/atom.

These considerations make it clear that the phase transitions are unlikely to be well described by a purely displacive mechanism. A more coherent picture can be found by instead considering order-disorder-type transitions. In this case thermal excitations cause the system to hop between different tilt configurations, corresponding to local minima on the PES. These tilt configurations can be simple ones, such as $a^-a^-c^+$, but the system also may sample more complicated tilt patterns corresponding to local minima. Here, successive octahedra are not necessarily exactly in phase or out of phase but form more complicated tilting patterns. The time-average structure that

emerges when the system samples the low-symmetry local minima is a phase of higher symmetry.

The critical temperature of an order-disorder transition depends on the height of the barriers on the minimum energy path between local minima on the PES. We saw in the previous section (Fig. 5) that there exist many paths between symmetry equivalent $a^-a^-c^+$ energy minima, all with very similar energy barriers. This fits into the picture of a single order-disorder transition where at the critical temperature many paths are available for the system to hop between symmetry equivalent minima on the PES. Since these minima are distributed symmetrically around the tiltless structure the time-averaged structure will be the ideal cubic perovskite.

We note again that it is the presence of tilts around several axes in the system that opens up paths on the PES which are low in energy since they do not pass over the cubic structure. This allows for the emergence of the cubic perovskite structure as a dynamical average at lower temperatures than what would be expected in a picture where the phase transition happens by a displacive mechanism. A similar situation was found for the tetragonal-to-cubic phase transition in ZrO_2 [51].

We also note that the important energy barriers in this case are not the depth of the double wells from *ip* and *oop* tilts in the cubic structure but the minimum energy paths between equivalent $a^-a^-c^+$ structures in Fig. 5.

It should be noted that, in general, it is rare that a phase transition can be identified uniquely as either order-disorder or displacive. It often shows some characteristics of both. In the present case it is likely that at temperatures moderately above the transition temperature, some tilt angles will actually thermally oscillate around zero. What is clear from the calculated potential-energy landscapes, however, is that at least one tilt has to be present in the system at these temperatures in order for the system to explicitly avoid the high-energy tiltless cubic configuration.

It is interesting to note that some hints of an order-disorder phase transition in CMO can be found in the experimental literature. In particular, Schrade *et al.* [52] indicated that, surprisingly, both the Seeback coefficient and the carrier mobility varied continuously across the orthorhombic-to-cubic phase transition. This is, in fact, a feature of an order-disorder transition since the reorientations of the octahedra take place on time scales much longer than those relevant to electronic properties. Thus, the effective electronic structure from the point of view of electronic conduction will be the same even across the phase transition.

We finally briefly discuss how the intermediate tetragonal phase may appear due to the presence of oxygen vacancies. The $a^-a^-c^+ \rightarrow a^-b^0b^0$ transition can be viewed straightforwardly as the order-disorder transition that occurs when the system samples the four minima in Fig. 4(b). This should, however, result in a structure with cubic symmetry since there is an identical potential-energy landscape as the one in Fig. 4 when the *oop* tilt around the pseudocubic *b* axis is fixed instead of the *a* axis. If, however, there are oxygen vacancies present in the system, and they have a tendency to order, this may induce a preferential axis in the system so that an *oop* tilt around this axis always is present whereas tilt switches around the two other axes occur. This would produce an average tetragonal $a^-b^0b^0$ structure. When the temperature is further increased this preferential axis will disappear, and the cubic structure will emerge as the time average. Such a vacancy ordering is, in fact, expected since the O vacancy formation energy of the two nonequivalent O ions in the *Pnma* structure is not equal

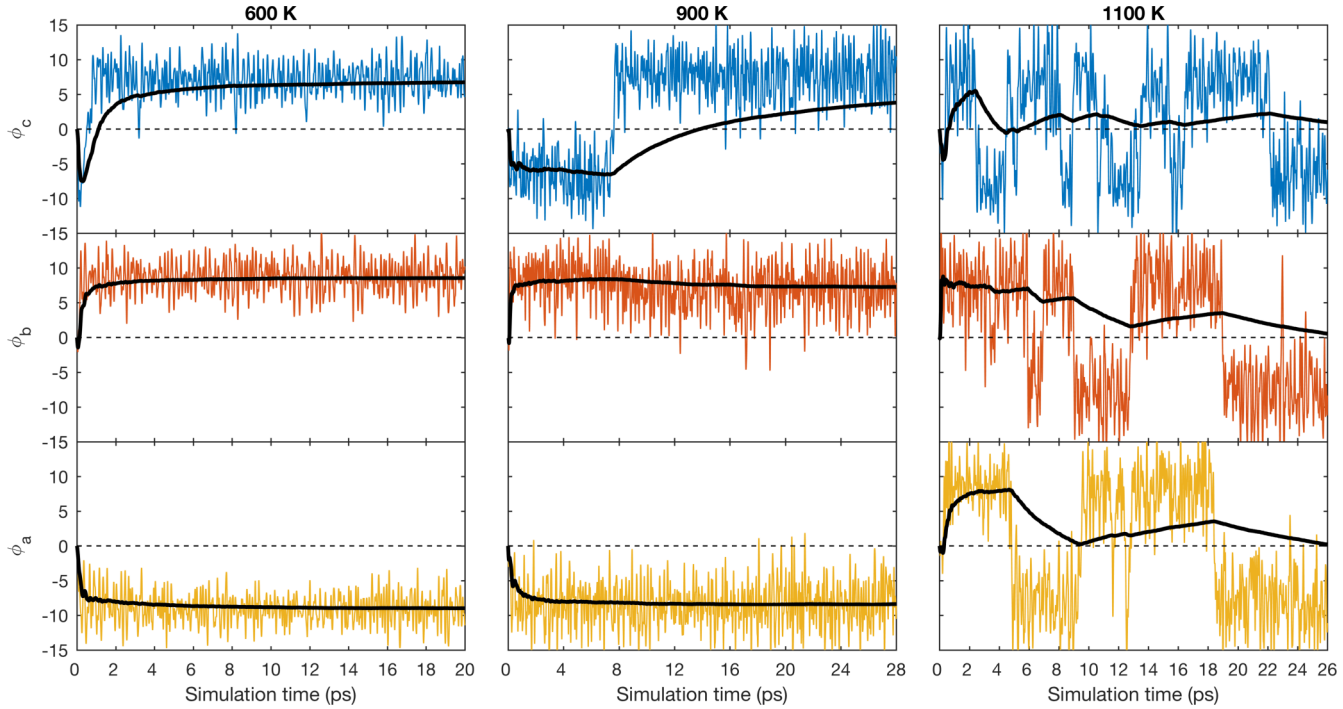

FIG. 6. Tilt angles ϕ_a, ϕ_b, and ϕ_c around the three pseudocubic axes for one selected octahedron as functions of simulation time at temperatures 600, 900 and 1100 K. The black lines correspond to the running average.

[53]. More detailed studies along these lines are beyond the scope of the present paper.

D. *Ab initio* molecular dynamics simulations

To gather explicit evidence for order-disorder-type dynamics in CMO we have performed a set of canonical (NVT) Born-Oppenheimer AIMD simulations.

We perform simulations at temperatures of 600, 900, and 1100 K. The tilt angles of all MnO_6 octahedra around the three pseudocubic axes are recorded as functions of time as described in Sec. II.

Figure 6 shows the tilt angles around the three pseudocubic axes of a single MnO_6 octahedron at 600, 900, and 1100 K. After being initiated in the ideal, tiltless, cubic positions with random velocities (normalized according to the Maxwell-Boltzmann distribution at the considered temperature), the octahedron instantly tilts around all three axes, confirming that the cubic structure is dynamically unstable at all three temperatures. At 600 K the structure finds the $a^-a^-c^+$ configuration after roughly 1 ps and then stays in it for the remainder of the simulation time. During the 900 K simulation we observe one single tilt switching event which is identified as a ($a^-a^-c^+ \rightarrow a^-b^+a^-$)-type transition. This single switching event may be considered as a precursor to the transition, happening at a higher temperatures. At 1100 K, however, the octahedron is found to perform many tilt switches in the investigated simulation time. Although the octahedron is clearly tilted along all three axes on the time scale of thermal oscillations, the running average (the black lines in Fig. 6) approaches zero for long times, and the average structure will thus appear to be the ideal tiltless perovskite. This result provides explicit confirmation of the conclusions we drew from the potential-energy landscapes and minimum energy paths in the previous sections.

In the $2 \times 2 \times 2$ repetition of the tetragonal unit cell used in our AIMD simulations, chains of MnO_6 octahedra along the pseudocubic a and b axes contain two octahedra that can tilt independently whereas such a chain in the c direction contains four independent octahedra. Since the octahedra are corner connected, the tilts in a plane orthogonal to the tilting axes are all fixed by specifying the tilt of a single octahedron. The full tilt configuration of the supercell can thus be specified by providing the tilts of all independent octahedra in one chain in each of the three pseudocubic directions. Figure 7 provides the tilt angles for the octahedra in three such chains for the simulation at 1100 K as functions of simulation time. It can be seen that the system preferentially resides in ($a^-a^-c^+$)-type configurations. Other tilt patterns along the c axis can also be identified, although their lifetimes are shorter, for instance, two octahedra tilted in one direction followed by two tilted in the other, indicating that this tilt configuration corresponds to a shallow minimum on the potential-energy surface. This particular tilt configuration does, in fact, carry some resemblance to the type of AFD domains that have been predicted to appear in CMO [54], although of much smaller domain size as limited by the supercell used in the AIMD simulations. A detailed analysis of the effect of AFD domains would be of interest but is beyond the scope of this paper.

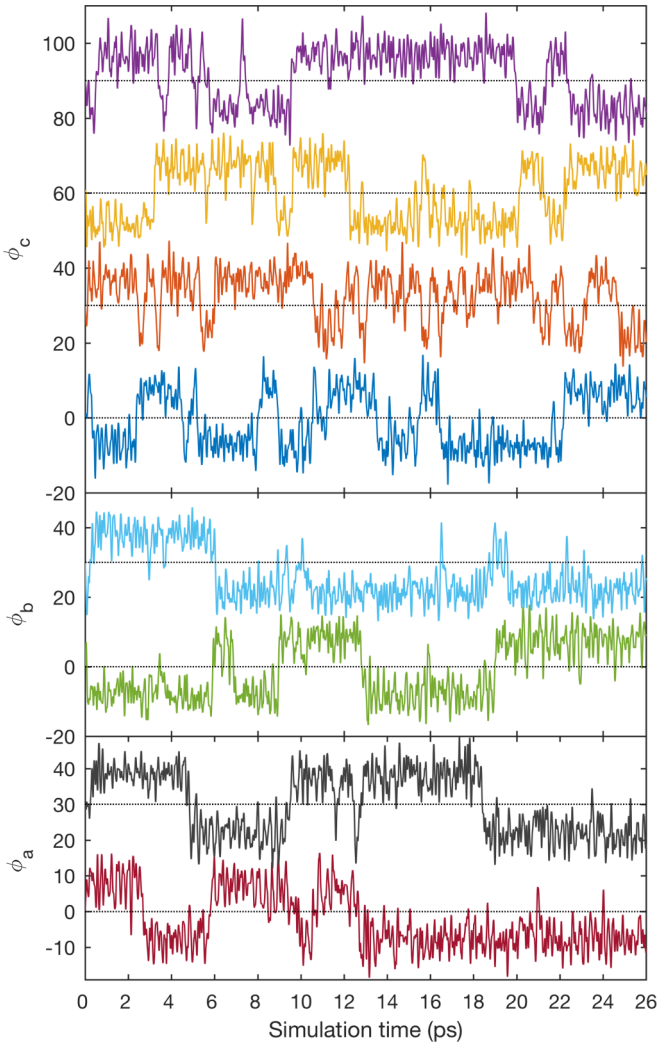

FIG. 7. Tilt angles ϕ_a, ϕ_b, and ϕ_c for a chain of octahedra in the a (lower panel), b (middle panel), and c (upper panel) pseudocubic directions. The data is from a simulation at $T = 1100$ K. For clarity, tilt angles of different octahedra have been offset vertically.

We invite future studies on the relation between order-disorder dynamics and AFD domains.

IV. CONCLUSIONS

To conclude, we have studied the temperature-induced structural phase transitions in CMO using first-principles density functional theory calculations. We have confirmed that the ideal cubic perovskite structure is dynamically unstable with respect to both ip and oop tiltings of MnO_6 octahedra, resulting in the orthorhombic $Pnma$ ground-state structure with Glazer tilt pattern $a^-a^-c^+$.

We have further studied the potential-energy landscapes generated from combinations of the unstable tilting modes. These calculations have revealed that having tilts around several pseudocubic axes present in the crystal allows for low-energy barrier paths between local minima on the potential-energy surface. The energy barriers on these paths are several times smaller than the ones passing over the high-energy tiltless cubic configuration. This implies that 1D double-well

potentials cannot be straightforwardly used to predict the nature (displacive or order-disorder) of AFD phase transitions in perovskites. Instead, the important energy barriers are those between symmetry equivalent minima on the PES that correspond to the ground-state structure, such as those in Fig. 5 in the case of CMO.

Based on our results we have argued that the structural phase transitions in CMO are best described by an order-disorder mechanism, i.e., when thermal excitations cause the system to hop via the low-energy paths between local minima on the potential-energy surface, yielding a high-symmetry structure on average. We have concluded that our results are consistent with a single $Pnma$-to-$Pm\bar{3}m$ transition. We have also pointed out that the intermediate tetragonal $I4/mcm$ phase may appear as a result of an ordering of oxygen vacancies, which naturally appears due to oxygen deficiency at high temperatures.

We have finally performed *ab initio* molecular dynamics simulations where we directly observe the hopping events, which provide direct evidence of the proposed order-disorder transition mechanism.

In general, we propose the following considerations that should be made when investigating the nature (displacive or order-disorder) of a sequence of octahedral tilting phase transitions in perovskites:

(1) Energy differences between two phases that are the end points of a tilting phase transition (such as $Pnma$ and $Pm\bar{3}m$ in the case of CMO) cannot be compared straightforwardly to the transition temperature as that might ignore the possibility of an order-disorder transition. The latter can proceed by hopping of the system between minima on the PES with energy barriers not related to the energy difference between the two phases.

(2) If the energy difference between the phases is much larger than the thermal energy at the experimentally determined transition temperature, this may indicate an order-disorder transition. In this case, paths between equivalent low-symmetry structures have to be identified, and the corresponding energy barriers should be calculated. In the typical case of the $Pnma$ structure examples of such paths are found in Fig. 5.

(3) If there exist such paths with energy barriers significantly lower than the energy differences between the two phases this is an indicator of a order-disorder transition mechanism. In addition, the existence of many distinct types of such paths (as, e.g., in CMO, see Fig. 5) is a further strong indicator of order-disorder behavior.

ACKNOWLEDGMENTS

The support from the Swedish Research Council (VR) (Project No. 2014-4750) and the Swedish Government Strategic Research Area in Materials Science on Functional Materials at Linköping University (Faculty Grant SFO-Mat-LiU No. 2009 00971) are acknowledged by S.I.S and J.K. Support from CeNano at Linköping University is acknowledged by J.K. The computations were performed on resources provided by the Swedish National Infrastructure for Computing (SNIC) at the PDC Centre for High Performance Computing (PDC-HPC), the National Supercomputer Center (NSC), and the Center for Scientific and Technical Computing (Lunarc).

[1] S. P. Jiang, J. Mater. Sci. **43**, 6799 (2008).
[2] A. Bhalla, R. Guo, and R. Roy, Mater. Res. Innovations **4**, 3 (2000).
[3] L. G. Tejuca and J. L. G. Fierro, *Properties and Applications of Perovskite-Type Oxides* (Dekker, New York, 1993).
[4] K. Koumoto, Y. Wang, R. Zhang, A. Kosuga, and R. Funahashi, Annu. Rev. Mater. Res. **40**, 363 (2010).
[5] M. A. Green, A. Ho-Baillie, and H. J. Snaith, Nat. Photonics **8**, 506 (2014).
[6] P. Thiel, S. Populoh, S. Yoon, G. Saucke, K. Rubenis, and A. Weidenkaff, J. Phys. Chem. C **119**, 21860 (2015).
[7] A. M. Glazer, Acta Crystallogr., Sect. B: Struct. Crystallogr. Cryst. Chem. **28**, 3384 (1972).
[8] M. T. Dove, Am. Mineral. **82**, 213 (1997).
[9] W. Zhong, D. Vanderbilt, and K. M. Rabe, Phys. Rev. B **52**, 6301 (1995).
[10] A. Bussmann-Holder, H. Beige, and G. Völkel, Phys. Rev. B **79**, 184111 (2009).
[11] A. L. Goodwin, S. A. T. Redfern, M. T. Dove, D. A. Keen, and M. G. Tucker, Phys. Rev. B **76**, 174114 (2007).
[12] L. Li, D. J. Weidner, J. Brodholt, D. Alfè, G. D. Price, R. Caracas, and R. Wentzcovitch, Phys. Earth Planet. Inter. **155**, 260 (2006).
[13] E. H. Mountstevens, S. A. T. Redfern, and J. P. Attfield, Phys. Rev. B **71**, 220102 (2005).
[14] R. E. A. McKnight, C. J. Howard, and M. A. Carpenter, J. Phys.: Condens. Matter **21**, 015901 (2009).
[15] M. K. Singh, N. K. Karan, R. S. Katiyar, J. F. Scott, and H. M. Jang, J. Phys.: Condens. Matter **20**, 055210 (2008).
[16] A. N. Beecher, O. E. Semonin, J. M. Skelton, J. M. Frost, M. W. Terban, H. Zhai, A. Alatas, J. S. Owen, A. Walsh, and S. J. L. Billinge, ACS Energy Lett. **1**, 880 (2016).
[17] H. Taguchi, M. Nagao, T. Sato, and M. Shimada, J. Solid State Chem. **78**, 312 (1989).
[18] G. Kresse and J. Furthmüller, Comput. Mater. Sci. **6**, 15 (1996).
[19] G. Kresse and J. Furthmüller, Phys. Rev. B **54**, 11169 (1996).
[20] G. Kresse and D. Joubert, Phys. Rev. B **59**, 1758 (1999).
[21] P. E. Blöchl, Phys. Rev. B **50**, 17953 (1994).
[22] J. Hong, A. Stroppa, J. Íñiguez, S. Picozzi, and D. Vanderbilt, Phys. Rev. B **85**, 054417 (2012).
[23] J. P. Perdew, A. Ruzsinszky, G. I. Csonka, O. A. Vydrov, G. E. Scuseria, L. A. Constantin, X. Zhou, and K. Burke, Phys. Rev. Lett. **100**, 136406 (2008).
[24] S. L. Dudarev, G. A. Botton, S. Y. Savrasov, C. J. Humphreys, and A. P. Sutton, Phys. Rev. B **57**, 1505 (1998).
[25] A. Togo and I. Tanaka, Scr. Mater. **108**, 1 (2015).
[26] D. Sheppard, P. Xiao, W. Chemelewski, D. D. Johnson, and G. Henkelman, J. Chem. Phys. **136**, 074103 (2012).
[27] J. Hubbard, Phys. Rev. B **19**, 2626 (1979).
[28] J. Hubbard, Phys. Rev. B **20**, 4584 (1979).
[29] J. Hubbard, Phys. Rev. B **23**, 5974 (1981).
[30] H. Hasegawa, J. Phys. Soc. Jpn. **46**, 1504 (1979).
[31] H. Hasegawa, J. Phys. Soc. Jpn. **49**, 178 (1980).

[32] D. M. Edwards, J. Phys. F **12**, 1789 (1982).
[33] T. Oguchi, K. Terakura, and N. Hamada, J. Phys. F **13**, 145 (1983).
[34] A. J. Pindor, J. Staunton, G. M. Stocks, and H. Winter, J. Phys. F **13**, 979 (1983).
[35] B. L. Gyorffy, A. J. Pindor, J. Staunton, G. M. Stocks, and H. Winter, J. Phys. F **15**, 1337 (1985).
[36] J. Staunton, B. L. Gyorffy, A. J. Pindor, G. M. Stocks, and H. Winter, J. Phys. F **15**, 1387 (1985).
[37] A. Zunger, S.-H. Wei, L. G. Ferreira, and J. E. Bernard, Phys. Rev. Lett. **65**, 353 (1990).
[38] P. Steneteg, B. Alling, and I. A. Abrikosov, Phys. Rev. B **85**, 144404 (2012).
[39] J. J. Neumeier, A. L. Cornelius, and K. Andres, Phys. Rev. B **64**, 172406 (2001).
[40] Q. Zhou and B. J. Kennedy, J. Phys. Chem. Solids **67**, 1595 (2006).
[41] S. Bhattacharjee, E. Bousquet, and P. Ghosez, Phys. Rev. Lett. **102**, 117602 (2009).
[42] S. K. Mishra, M. K. Gupta, R. Mittal, A. I. Kolesnikov, and S. L. Chaplot, Phys. Rev. B **93**, 214306 (2016).
[43] A. Marthinsen, C. Faber, U. Aschauer, N. A. Spaldin, and S. M. Selbach, MRS Commun. **6**, 182 (2016).
[44] R. X. Yang, J. M. Skelton, E. L. da Silva, J. M. Frost, and A. Walsh, J. Phys. Chem. Lett. **8**, 4720 (2017).
[45] H. Sim and B. G. Kim, Phys. Rev. B **89**, 201107 (2014).
[46] P. Thiel, S. Populoh, S. Yoon, and A. Weidenkaff, J. Solid State Chem. **229**, 62 (2015).
[47] E. I. Leonidova, I. A. Leonidov, M. V. Patrakeev, and V. L. Kozhevnikov, J. Solid State Electrochem. **15**, 1071 (2011).
[48] P. Thiel, J. Eilertsen, S. Populoh, G. Saucke, M. Döbeli, A. Shkabko, L. Sagarna, L. Karvonen, and A. Weidenkaff, J. Appl. Phys. **114**, 243707 (2013).
[49] L. Bocher, M. H. Aguirre, R. Robert, D. Logvinovich, S. Bakardjieva, J. Hejtmanek, and A. Weidenkaff, Acta Mater. **57**, 5667 (2009).
[50] C. J. Howard, K. S. Knight, B. J. Kennedy, and E. H. Kisi, J. Phys.: Condens. Matter **12**, L677 (2000).
[51] C. Carbogno, C. G. Levi, C. G. Van de Walle, and M. Scheffler, Phys. Rev. B **90**, 144109 (2014).
[52] M. Schrade, R. Kabir, S. Li, T. Norby, and T. G. Finstad, J. Appl. Phys. **115**, 103705 (2014).
[53] U. Aschauer, R. Pfenninger, S. M. Selbach, T. Grande, and N. A. Spaldin, Phys. Rev. B **88**, 054111 (2013).
[54] P. Barone, D. Di Sante, and S. Picozzi, Phys. Rev. B **89**, 144104 (2014).